

# Solutions of the converging and diverging shock problem in a medium with varying density

Itamar Giron, Shmuel Balberg, and Menahem Krief\*

*Racah Institute of Physics, The Hebrew University, 9190401 Jerusalem, Israel*

We consider the solutions of the Guderley problem, consisting of a converging and diverging hydrodynamic shock wave in an ideal gas with a power law initial density profile. The self-similar solutions, and specifically the reflected shock coefficient, which determines the path of the reflected shock, are studied in detail, for cylindrical and spherical symmetries and for a wide range of values of the adiabatic index and the spatial density exponent. Finally, we perform a comprehensive comparison between the analytic solutions and Lagrangian hydrodynamic simulations, by setting proper initial and boundary conditions. A very good agreement between the analytical solutions and the numerical simulations is obtained. This demonstrates the usefulness of the analytic solutions as a code verification test problem.

## I. INTRODUCTION

The Guderley problem is a well known hydrodynamic problem of a strong shock propagating radially in an ideal gas medium. The shock originates at infinity and collapses to a central point or an axis, where it is reflected and diverges towards infinity [1–9]. The problem was first formulated with an initially uniform density profile, and was analyzed comprehensively and solved for this case by Lazarus **and Richtmyer** [2, 3]. The theory of converging and diverging compressible shocks is an active research area, where for example, the Guderley problem was generalized to include: non-ideal equations of state [10–15], magneto-hydrodynamics [16, 17], and gravitation [18]. Recently, a general solution for continuous converging waves was developed [19].

Imploding shocks are often invoked as a possible ignition mechanism in reactive material. These include chemical compounds (see Ref. [20] for a review on laboratory experiments), and thermonuclear, in inertial confinement fusion experiments [21, 22] and detonation in white dwarfs in astrophysics [23, 24]. A fundamental feature in such ignition scenarios is that both the converging and diverging shocks may lead to ignition, since the particulars depend on a competition between the hydrodynamical time and the heating time due to the exothermal burning processes. Interestingly, the critical strength of the shock required to reach ignition is usually determined by the diverging shock. While this shock is typically not strong (as opposed to the earlier converging shock), the post-shock material in this stage has higher densities and temperatures, having being shocked twice; see the analytical and numerical analysis by [23]. Hence, an accurate calculation of the entire converging-diverging shock sequence is crucial to understanding (and designing) an ignition candidate system.

In Ref. [25] we presented generalized solutions for the converging shock for a power law initial density profile

$\rho(r) \sim r^\mu$ , with a general spatial exponent  $\mu$  (see also [6, 7, 26, 27]). In this work we extend this generalization of the initial density profile, to the reflected diverging shock solution. By combining the solutions for the converging and diverging flows we obtain a solution of the complete Guderley problem for an initial power law density profile.

The Guderley problem is a self-similar problem of the second kind, in which the similarity is found by requiring the solution to pass through a singularity, such as a sonic point. As a result, its solution is given in terms of similarity profiles as the hydrodynamic Euler equations are transformed into a system of ordinary differential equations (ODE). An extension of the problem to a general power law initial density is possible, since this generalization does not introduce additional dimensional parameters to the problem [28–31]. The equations describing the similarity profiles contain two unknown parameters which need be determined, either approximately [32, 33] using simple analytical methods, or exactly using more sophisticated numerical methods. An exact numerical method for the calculation of the first parameter, the similarity exponent  $\lambda$  was developed for general  $\mu$ , in our previous work [25]. The second parameter, which is the diverging shock constant  $B$ , was calculated in the literature for  $\mu = 0$  by Lazarus et. al [2–4] and Ramsey et. al [4].

The Guderley problem can be used as a nontrivial test problem for hydrodynamic simulation codes [4, 8, 10, 25, 34–37]. Using the generalized semi-analytic solutions, we define two types of test problems for hydrodynamic simulation codes, by properly defining the initial and boundary conditions. The tests represent the dynamics of the diverging shock as well as the dynamics of both the converging and diverging shock in the same simulation. We perform a detailed comparison between the simulations and the analytic solutions, for a variety of  $\gamma$  (the ideal gas adiabatic index) and  $\mu$ .

In this work we focus on the calculation of the diverging shock. We generalize the method of Lazarus [3] and present a robust method for the calculation of the diverging shock constant  $B$ , for a general value of the initial density exponent  $\mu$ . The structure of the article is as

---

\* menahem.krief@mail.huji.ac.il

follows. In section II we review the generalized Guderley problem and its self-similar solutions for the converging and diverging shocks are presented. In section III a robust method for the calculation of the diverging shock constant and the resulting similarity profiles, for general values of  $\mu$  is developed. The solutions are calculated for a wide range of values of  $\gamma$  and  $\mu$ , and are compared to the results of previously published works when such exist. In section IV we define two types of test problems for hydrodynamic simulation codes, by properly defining the initial and boundary condition of a piston with velocity given from the analytic solution [36]. We perform detailed hydrodynamic simulations and compare the results to the similarity solutions. We conclude in section V.

## II. THE GUDERLEY PROBLEM

In this work we consider the hydrodynamic problem of a shock wave which diverges to infinity in an ideal gas medium. This diverging shock is originated by a previously converging shock wave according to the Guderley problem, which has reached the origin and reflected from a central point (spherical symmetry) or an axis (cylindrical symmetry), as demonstrated in figures 1-2.

For completeness, we list again the governing equations and employ the same notation as in Ref. [25]. The Euler equations which describe the compressible gas flow are:

$$\frac{1}{\rho} \frac{\partial \rho}{\partial t} + \frac{u}{r} \frac{\partial \rho}{\partial r} + \frac{\partial u}{\partial r} + (n-1) \frac{u}{r} = 0, \quad (1)$$

$$\frac{\partial u}{\partial t} + u \frac{\partial u}{\partial r} + \frac{c^2}{\gamma \rho} \frac{\partial \rho}{\partial r} + 2c \frac{\partial c}{\partial r} = 0, \quad (2)$$

$$\frac{\partial c}{\partial t} + u \frac{\partial c}{\partial r} + \frac{(\gamma-1)c}{2} \left( \frac{\partial u}{\partial r} + \frac{(n-1)u}{r} \right) = 0, \quad (3)$$

where  $\rho(r, t)$  denotes the fluid density,  $u(r, t)$  the velocity,  $c(r, t)$  the sound speed, and  $n$  the symmetry dimension ( $n = 2$  for cylindrical axial symmetry and  $n = 3$  for spherical symmetry). The medium is assumed to consist of an ideal gas with an adiabatic index  $\gamma$ , so that the equation of state is:

$$p(\rho, e) = (\gamma - 1) \rho e, \quad (4)$$

relating the pressure  $p$  to the specific internal energy  $e$  and density  $\rho$ . The sound speed is then:

$$c = \sqrt{\frac{\gamma p}{\rho}}. \quad (5)$$

A converging Guderley shock is originated at  $r = \infty$  and  $t = -\infty$ , and propagates in a cold material which is at

rest and whose initial density profile has a spatial power law of the form [25]:

$$\rho(r, t = -\infty) = \rho_0 r^\mu. \quad (6)$$

We note that for  $\mu < 0$  the density diverges at  $r = 0$ , and henceforth we limit ourselves to the constraint  $\mu \geq -n$  in order for the total mass enclosed by finite radii to be finite as well. It is noteworthy that this choice limits us to the physical regime where the converging shock must reach the center; there does exist a critical value  $\mu_b < -n$  for which the shock does not converge due to the step density gradient towards the origin. Similarly, we also limit our analysis to values  $\mu < \mu_c$ , which is a positive critical value, for which steeper outward-increasing density profiles will cause the diverging shock to stall. See [27] for a derivation of  $\mu_b, \mu_c$  as a function of dimension and  $\gamma$ .

The Rankine-Hugoniot jump relations relate the values of the thermodynamic quantities across the shock:

$$D(\rho_2 - \rho_1) = \rho_2 u_2 - \rho_1 u_1, \quad (7)$$

$$p_1 + \rho_1 (u_1 - D)^2 = p_2 + \rho_2 (u_2 - D)^2, \quad (8)$$

$$e_1 + \frac{p_1}{\rho_1} + \frac{1}{2} (u_1 - D)^2 = e_2 + \frac{p_2}{\rho_2} + \frac{1}{2} (u_2 - D)^2, \quad (9)$$

where  $D$  is the shock velocity, and the indices 1 and 2 correspond to the pre-shocked and post-shocked components, respectively. The solution of the converging shock is described via a self-similar representation at negative times, so that incoming shock position is given as a temporal power law:

$$r_{\text{in-shock}}(t) = (-t)^{\frac{1}{\lambda}}, \quad (10)$$

where  $\lambda$  is the similarity exponent. The independent similarity variable  $x$ , is defined by:

$$x = \frac{t}{r^\lambda}. \quad (11)$$

The similarity functions for the velocity, sound-speed and density profiles,  $V(x)$ ,  $C(x)$  and  $R(x)$  are defined, respectively, as:

$$u(r, t) = -\frac{r}{\lambda t} V(x), \quad (12)$$

$$c(r, t) = -\frac{r}{\lambda t} C(x), \quad (13)$$

$$\rho(r, t) = \rho_0 r^\mu R(x). \quad (14)$$

Substituting of the self-similar representation (12)-(14) in the Euler equations (1)-(3), results in a system of ordinary differential equations (ODEs) for the similarity profiles :

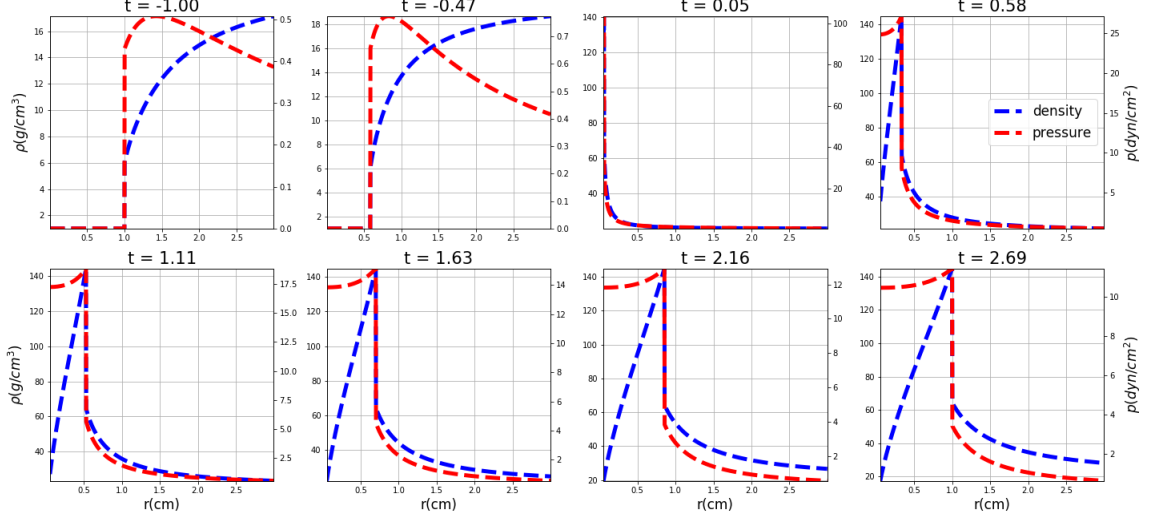


Figure 1. The density (blue) and pressure (red) profiles of the converging and diverging shock problem, at various times which are listed in the titles (time is ordered by: left to right, top to bottom). The converging shock is originated at  $r = \infty$ ,  $t = -\infty$ , and reaches the point  $r = 1$  at time  $t = -1$ . Subsequently it converges at the center  $r = 0$  at time  $t = 0$  and then reflects as a diverging shock which propagates outwards, reaching the point  $r = 1$  at  $t = B$  (see equation 21). The case shown is for  $\rho_0 = 1\text{g/cm}^3$  and the parameters  $\mu = 0$  (an initially homogeneous density),  $\gamma = 1.4$ ,  $n = 3$  (spherical symmetry), for which  $\lambda = 1.3944$  and  $B = 2.6885$ .

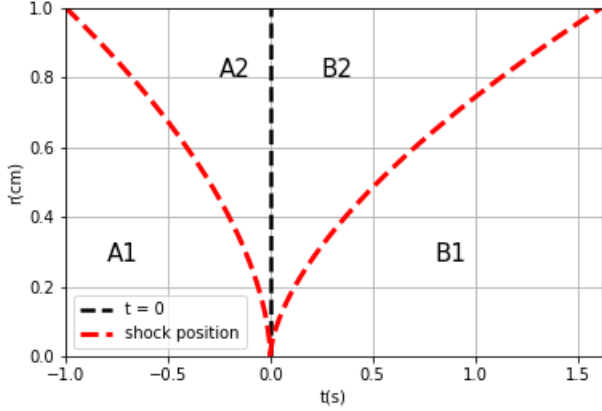


Figure 2. The converging and diverging shock positions as a function of time, for the case  $\gamma = 2$ ,  $\mu = 1$ ,  $n = 3$ , for which  $\lambda = 1.7498$ ,  $B = 1.6189$ . The  $r - t$  plane is split into four regions: (**A1**) is the undisturbed region in the converging shock case, (**A2**) is the shocked region in the converging shock problem, (**B1**) is the region shocked by the diverging shock and (**B2**) is the region in front of the diverging shock. In the previous work [25] the incoming shock regions **A1**, **A2** were examined. This work focuses on the outgoing shock regions **B1**, **B2**.

$$\mathbf{A} \frac{d}{dx} \begin{bmatrix} R \\ V \\ C \end{bmatrix} = \begin{bmatrix} V(\mu + n) \\ R(C^2(2 + \mu) + \gamma V(\lambda + V)) \\ \frac{C(2(V + \lambda) + n(\gamma - 1))}{2\gamma(1 + V)} \end{bmatrix}, \quad (15)$$

where  $\mathbf{A}$  is the matrix:

$$\mathbf{A} = \lambda x \begin{bmatrix} \frac{1+V}{R^2} & 1 & 0 \\ C^2 & \gamma R(V+1) & 2RC \\ 0 & \frac{C(\gamma-1)}{2\gamma(V+1)} & \frac{1}{\gamma} \end{bmatrix}.$$

Finally, solving for the derivatives gives the canonical ODE form:

$$\lambda x R' = \frac{\Delta_1}{\Delta}, \quad \lambda x V' = \frac{\Delta_2}{\Delta}, \quad \lambda x C' = \frac{\Delta_3}{\Delta}, \quad (16)$$

with the following determinants:

$$\Delta(V, C) = C^2 - (V + 1)^2, \quad (17)$$

$$\Delta_1(R, V, C, \lambda, \mu) = R \left[ \frac{2(1 - \lambda) + \mu(\gamma V + 1)}{\gamma(V + 1)} C^2 + V(V + \lambda) - (n + \mu)V(V + 1) \right], \quad (18)$$

$$\Delta_2(V, C, \lambda, \mu) = C^2 \left( nV + \frac{2(\lambda - 1) - \mu}{\gamma} \right) - V(V + 1)(V + \lambda), \quad (19)$$

$$\Delta_3(V, C, \lambda, \mu) = C \left[ C^2 \left( 1 + \frac{2(\lambda - 1) + \mu(\gamma - 1)}{2\gamma(1 + V)} \right) - (V + 1)^2 - (n - 1)(\gamma - 1) \frac{V(1 + V)}{2} - (\lambda - 1) \frac{(3 - \gamma)V + 2}{2} \right]. \quad (20)$$

We note that the typographical error in equation 16 of Ref. [25] is now corrected in equation 17 (the order of the terms on the right hand side was corrected).

The imploding shock reaches the center at time  $t = 0$ , and is then reflected into a diverging shock which propagates outward. As shown by Lazarus in Refs. [2, 3], the diverging shock position has the same similarity exponent  $\lambda$ , so that the converging and diverging shock positions are written as (see figure 2):

$$r_{\text{shock}}(t) = \begin{cases} (-t)^{\frac{1}{\lambda}} & t \leq 0 \\ (\frac{t}{B})^{\frac{1}{\lambda}} & t > 0 \end{cases} \quad (21)$$

where  $B = B(\gamma, \mu, n)$  is a constant which represents the time it takes the outgoing shock to travel from  $r = 0$  to  $r = 1$ , and depends only on the defining quantities in the problem:  $\gamma, \mu, n$ . In Ref. [25] we discussed in detail how to calculate the similarity exponent  $\lambda(\gamma, \mu, n)$  using iterative methods. In the following we complete the derivation with an analytic solution for the diverging shock, for which we develop in detail a method for calculating  $B(\gamma, \mu, n)$ .

### III. CALCULATION OF $B(\gamma, \mu, n)$

In this section we describe a robust method for calculating the parameter  $B$  using iterative algorithms. We generalize the method of Lazarus [2, 3], which dealt with the specific case of an initially homogeneous density ( $\mu = 0$ ), to a general power law density (equation 6). In section III A we describe the proper integration path for equation 16, which in turn, gives a constraint which enables the calculation of the constant  $B$ . This method resembles the calculation of the similarity exponent  $\lambda$ , which is determined by a constraint on the integration path for the incoming shock, as it crosses a singular point [25].

#### A. The Integration Path

The full integration path for the converging and diverging shock in the  $C - V$  plane is outlined and described in detail in figure 3. As discussed above, the diverging shock we consider here was generated by a previously converging Guderley shock. As a result, the full integration path of equation 16 should first pass through the

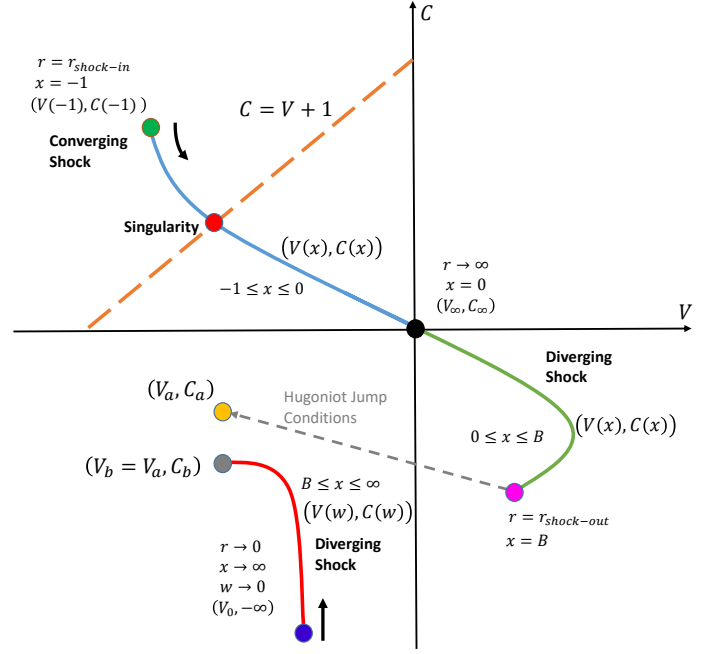


Figure 3. The integration path of the similarity ODEs (equation 16) in the  $C - V$  plane. The integration starts (green point) at the converging shock front where  $x = -1$  (equations 22, 24), then goes through the singularity (which is removable by definition of the similarity exponent  $\lambda$ , as detailed in Ref. [25]), and reaches  $x = 0$  ( $r = \infty$  of the converging shock profile), as described by the blue curve. At this point (black point, where  $x = V = C = 0$ ), the integration switches to positive times ( $x \geq 0$ ) and represents the diverging shock. It extends (green curve) until it reaches the diverging shock front at  $x = B$  (magenta point). The properties of material on the other side of this front are then found through the Rankine-Hugoniot jump conditions (equations 25-27), and we obtain the point  $(V_a, C_a)$  (yellow point). Finally, we define another integration variable  $w = x^{-\sigma}$  (as detailed in the text) and integrate the ODEs 34-35 to this shock front, from the origin  $(V_0, -\infty)$  (blue point,  $V_0$  given by equation 31), and continue (red curve) to the shock front until the value  $V(w) = V_a$  is reached. This integration will end at some value  $C(w) = C_b$ , (gray point), and the correct value of the parameter  $B$  is such that  $C_a = C_b$ .

integration path of the incoming shock [25], and in particular it should start from the incoming shock front coordinate,  $x = -1$ , where the strong shock Rankine-Hugoniot relations give the following values for the similarity profiles at the front [25]:

$$V(-1) = -\frac{2}{\gamma + 1}, \quad (22)$$

$$R(-1) = \frac{\gamma + 1}{\gamma - 1}, \quad (23)$$

$$C(-1) = \frac{\sqrt{2\gamma(\gamma - 1)}}{\gamma + 1}. \quad (24)$$

The integration is continued all the way to  $x = 0$  where  $(V, C) = (0, 0)$ . At this point, the integration continues consistently to positive  $x$ , which represents the diverging shock from  $r \rightarrow \infty$  and inwards, and is evaluated at positive times. The integration terminates at the diverging shock front, which (equations 11,21) corresponds to  $x = B$ . Therefore integration of equations 16 from the incoming shock front at  $x = -1$  to  $x = B$  will give the similarity profiles through the diverging shock as well, terminating at where the solution is discontinuous according to the Rankine–Hugoniot jump relations (equations 7-9). These relations can be written in terms of the similarity profiles, by substituting equations 12-14 into jump relations, as derived in detail in Appendix A (see also Ref. [3]). Again denoting and the indices 1 and 2 correspond to the pre-shocked and post-shocked components by  $(R_1, V_1, C_1)$  and  $(R_2, V_2, C_2)$ , respectively, the resulting Rankine-Hugoniot jump relations are:

$$1 + V_2 = \frac{\gamma - 1}{\gamma + 1} (1 + V_1) + \frac{2C_1^2}{(\gamma + 1)(1 + V_1)}, \quad (25)$$

$$R_2 (1 + V_2) = R_1 (1 + V_1). \quad (26)$$

$$C_2^2 = C_1^2 + \frac{\gamma - 1}{2} \left( (1 + V_1)^2 - (1 + V_2)^2 \right), \quad (27)$$

We note that that in the case of the diverging shock we need to solve for nonzero pressure in the upstream material, since it has been affected by the converging shock (which in itself has been treated as strong, propagating into cold gas) (See figures 1-2). After the jump at  $x = B$  via equations 25-27, the integration path should continue from  $x = B$  and  $(R_2, V_2, C_2)$  to  $x = \infty$  ( $r \rightarrow 0$ ,  $t > 0$ ).

In order to perform this integration numerically, we first calculate the asymptotic values of  $V, C$  for  $x \rightarrow \infty$ . From symmetry arguments the velocity at the center must vanish, that is  $u(r \rightarrow 0, t) = 0$ . As a result, from the definition of the velocity similarity profile  $V(x)$  (equation 12) we find,

$$\lim_{x \rightarrow \infty} x^{-\frac{1}{\lambda}} V(x) = 0. \quad (28)$$

Since the speed of sound is always finite and positive for  $r \rightarrow 0$ , it follows from the definition of  $C(x)$  (equation 13) that:

$$\lim_{x \rightarrow \infty} C(x) = -\infty. \quad (29)$$

If we now write the ODE for  $V(x)$  at  $x \rightarrow \infty$ , we obtain:

$$\begin{aligned} \frac{dV}{dx} &= \frac{C^2 \left( nV + \frac{2(\lambda-1)-\mu}{\gamma} \right) - V(V+1)(V+\lambda)}{\lambda x (C^2 - (V+1)^2)} \\ &\approx \frac{C^2 \left( nV + \frac{2(\lambda-1)-\mu}{\gamma} \right)}{\lambda x C^2} = \frac{nV + \frac{2(\lambda-1)-\mu}{\gamma}}{\lambda x} \end{aligned}$$

This results in a simple ODE whose solution is given by

$$V(x) = V_0 + Ax^{\frac{n}{\lambda}}, \quad (30)$$

where:

$$V_0 = -\frac{2(\lambda-1)-\mu}{n\gamma}, \quad (31)$$

and  $A$  is an integration constant. From equation 28 and since  $n \geq 1$  it follows that we must have  $A = 0$ , so we obtain the result:

$$\lim_{x \rightarrow \infty} V(x) = V_0. \quad (32)$$

Equations 29,32 gives the asymptotic behavior for  $V, C$  for  $x \rightarrow \infty$ . Following Lazarus [2, 3], in order to properly handle the integration near  $x \rightarrow \infty$ , we perform the following change of variables:

$$w = kx^{-\sigma}, \quad (33)$$

with a specific value for  $\sigma > 0$  which will be determined shortly. We use the relation  $\lambda x \frac{d}{dx} = -\lambda \sigma w \frac{d}{dw}$  in equation 16 and obtain ODEs for  $C(w), V(w)$ :

$$\lambda \sigma w \frac{dV}{dw} = -\frac{\Delta_2}{\Delta}, \quad (34)$$

$$\lambda \sigma w \frac{dC}{dw} = -\frac{\Delta_3}{\Delta}, \quad (35)$$

which depends on  $\sigma$  but not on the value of  $k$ . According to equation 29, we expand  $C(w)$  around  $w = 0$  (which corresponds to  $x \rightarrow \infty$ ):

$$C(w) = \dots + \frac{C_{-2}}{w^2} + \frac{C_{-1}}{w} + C_0 + C_1 w \dots \quad (36)$$

Writing equation 35 explicitly (using equations 17,20) in the limit  $w \rightarrow 0$ , leads to,

$$\frac{dC}{dw} = -\frac{C(w)}{w\lambda\sigma} \left( 1 + \frac{2(\lambda-1) + \mu(\gamma-1)}{2\gamma(1+V(w))} \right).$$

Inserting the expansion 36 and taking the limit  $w \rightarrow 0$  yields,

$$\begin{aligned} \dots - \frac{2C_{-2}}{w^3} - \frac{C_{-1}}{w^2} &= -\frac{1}{\lambda\sigma} \left( 1 + \frac{2(\lambda-1) + \mu(\gamma-1)}{2\gamma(1+V_0)} \right) \\ &\times \left( \dots + \frac{C_{-2}}{w^3} + \frac{C_{-1}}{w^2} + \frac{C_0}{w} \right). \end{aligned}$$

We see that at every order  $l \leq -1$  we must have:

$$lC_l = -\frac{1}{\lambda\sigma} \left( 1 + \frac{2(\lambda-1) + \mu(\gamma-1)}{2\gamma(1+V_0)} \right) C_l. \quad (37)$$

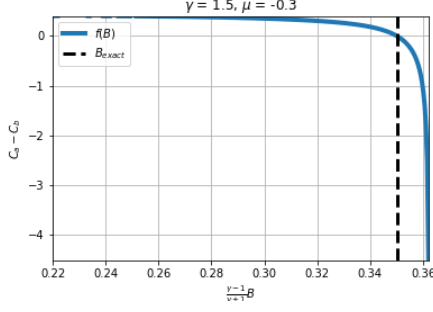


Figure 4. The difference between the dimensionless sound speed from both sides of the integration (blue curve), as a function of  $\frac{\gamma-1}{\gamma+1}B$  (as described in Sec. IIIB), for  $\gamma = 1.5$ ,  $\mu = -0.3$ ,  $n = 3$ . This difference vanishes for the correct value of  $B$  (vertical black line).

Hence only one value of  $l$  can satisfy equation 37 with  $C_l \neq 0$ , depending on the value of  $\sigma$ . As a result, by taking:

$$\sigma = \frac{1}{\lambda} \left( 1 + \frac{2(\lambda - 1) + \mu(\gamma - 1)}{2\gamma(1 + V_0)} \right), \quad (38)$$

we set  $l = -1$  with  $C_{-1} \neq 0$ , while  $C_l = 0$  for all  $l \leq -2$ . Finally, the value of  $k$  can thus be set such that  $C_{-1} = 1$ . In summary, with the choice of equation 38, we have:

$$C(w \rightarrow 0) \approx -\frac{1}{w} \quad (39)$$

### B. Numerical bracketing of $B$

The key to the full solution of the diverging shock is to determine the correct value of the parameter  $B$ , which we do iteratively. As described in figure 3 which depicts the integration path in the  $C - V$  plane, for a given trial value of  $B$  the ODEs 16 are integrated from  $x = -1$  to  $x = B$ , and then using the jump conditions we obtain  $V_2, C_2$  from equations 25,27 which we denote as  $(V_a, C_a)$ .

In the next step, the ODEs are integrated from the other direction ( $x \rightarrow \infty$ ) towards  $x = B$ . This is done by switching the integration variable to  $w$  (equation 33) and integrating equations 34-35 from some point  $w_0 \ll 1$  with the initial values  $(V, C) = (V_0, \frac{1}{w_0})$ , according to the asymptotic relations 30,39. In practice we take  $w_0 = 10^{-7}$ . The integration is carried out until the value  $V(w) = V_a$  is reached. The value of  $C(V_a)$  obtained at the end of the integration on  $w$  is denoted by  $C_b$ . If the correct value of  $B$  is used, the integration from both sides will meet at the same point in the  $C - V$  plane (figure 3), that is, we must have  $C_a = C_b$ .

This method allows for a robust calculation of  $B$ , by numerically bracketing the root of the function  $f(B) = C_a - C_b$ , as shown in figure 4. In order to set an initial

$\gamma = \frac{5}{3}$		
$\mu$	$B_{n=2}$	$B_{n=3}$
-1.0	0.83233629	0.92183037
-0.684210	1.03899820	1.08282717
-0.526315	1.16539327	1.17631586
0.263157	2.02484184	1.76890317
0.736842	2.74231348	2.23013019
$\gamma = 1.4$		
$\mu$	$B_{n=2}$	$B_{n=3}$
-1.0	1.14084671	1.38075188
-0.684210	1.54284404	1.71998084
-0.526315	1.78569523	1.91403860
0.263157	3.47396741	3.15677630
0.4210526	3.92133697	3.46678822

Table I. Various values of  $B$  for  $\gamma = \frac{5}{3}, 1.4$  for different values of  $\mu$  for cylindrical ( $n = 2$ ) and spherical ( $n = 3$ ) symmetries.

range  $[B_{\min}, B_{\max}]$  for the the bracketing, we found that for a wide range of  $\gamma$  and  $\mu$ :

$$0 \leq \frac{\gamma - 1}{\gamma + 1} B(\gamma, \mu, n) \leq 2 \quad (40)$$

(this formula is an extension of that found by Lazarus [3] for  $\mu = 0$ , with 1 on the right hand side of the inequality).

In order to set the initial bracketing range  $[B_{\min}, B_{\max}]$  such that  $f(B_{\min}) \cdot f(B_{\max}) < 0$ , we linearly scan the segment  $[0, 2\frac{\gamma+1}{\gamma-1}]$  until we find  $B_{\min}, B_{\max}$  which result in different signs of  $f(B)$ . After finding  $B_{\max}$  and  $B_{\min}$  we use a standard bisection method to bracket the root  $B$ . Some caution is necessary, since  $C_a - C_b$  may diverge for certain values of  $B$ , as shown in figure 4. If such divergence occurs, we reduce the scanning increment  $\Delta B$  and repeat the process from the last successful iteration,  $B_*$ , until once again we find an appropriate range of  $[B_{\min}, B_{\max}]$ .

### C. Integration of the Self-Similar Profiles

As described in figure 3, after the correct value of  $B$  is determined, we can integrate 16 to obtain the semi-analytic self-similar profiles  $V(x), C(x), R(x)$ . The integration starts from  $x = -1$  with the (converging) strong shock conditions:

$$(V, C, R) \Big|_{x=-1} = \left( -\frac{2}{\gamma+1}, \frac{\gamma+1}{\gamma-1}, \frac{\sqrt{2\gamma(\gamma-1)}}{\gamma+1} \right),$$

and continues to  $x = 0$  to the values representing the diverging shock,  $t > 0$ , and  $x \geq 0$ . From this point the solution represents the diverging shock from  $r \rightarrow \infty$  to the diverging shock front. At the shock front  $x = B$ , we use the jump conditions 26-27 and continue the

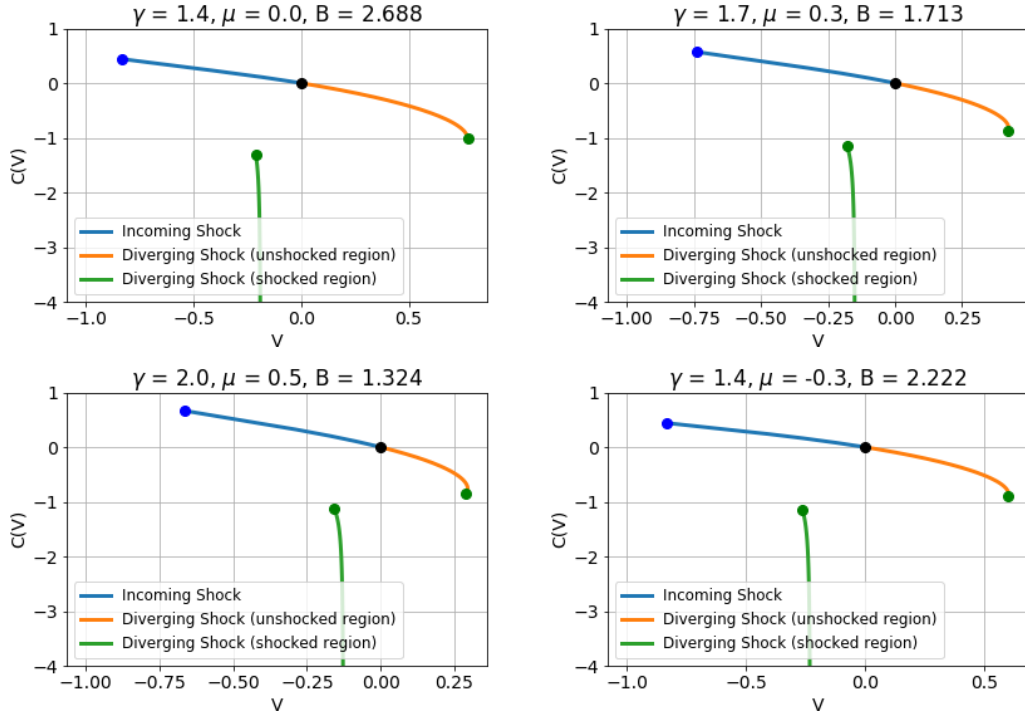


Figure 5. The curves  $C(V)$  of four different cases in spherical symmetry - the parameters and the resulting values of  $B$  are listed in the titles. The integration of  $C(V)$  in the  $C-V$  plane (as described in detail in figure 3), is divided into 3 regions: (i) the blue curve represents the converging shock from the shock front to  $r \rightarrow \infty$ , (ii) the orange curve represents the upstream flow from  $r \rightarrow \infty$  to the diverging shock front and (iii) the green curve represents the downstream flow from the diverging shock front to the center  $r = 0$ .

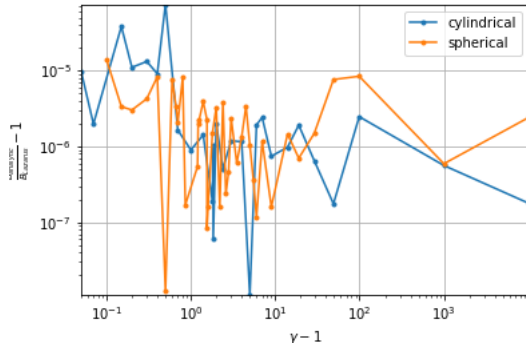


Figure 6. The relative error between the values of  $B$  calculated with our algorithm and values found by Lazarus for  $\mu = 0$  [3], as a function of  $\gamma - 1$ , for cylindrical (blue) and spherical (orange) symmetries.

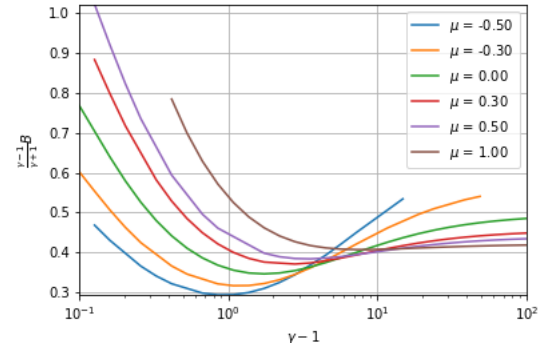


Figure 7.  $\frac{\gamma-1}{\gamma} B$  as a function of  $\gamma$  for different values of  $\mu$  (as listed in the legend) and in spherical symmetry.

## D. Results

integration to  $x \rightarrow \infty$  ( $r \rightarrow 0$ ). In practice we integrate on a finite range  $x \leq x_\infty$ , which is truncated at:

$$x_\infty = \frac{t}{r_{\min}^\lambda}$$

where we take  $r_{\min} = 0.05$ .

In figure 5 we plot the curve  $C(V)$  for several cases, as obtained from the numerical integration described in figure 3. To the best of our knowledge, numerical results for the values of  $B$  appear in the literature only for  $\mu = 0$ . In this case, the values published by Lazarus [3] are used as a benchmark to evaluate the algorithm - as was done for example in Ref. [4]. Thus we compare our results for

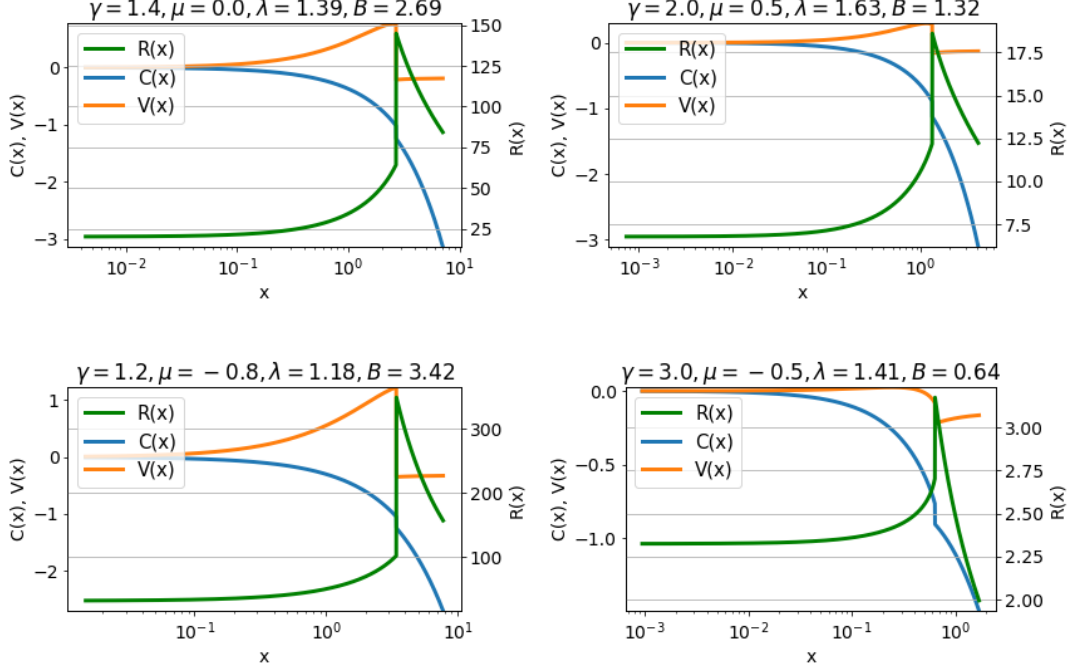


Figure 8. The self-similar profiles  $V(x)$  (orange, left  $y$ -axis),  $C(x)$  (blue, left  $y$ -axis) and  $R(x)$  (green, right  $y$ -axis) as a function of  $x$ , for four different cases in spherical symmetry - the parameters and the resulting values of  $B, \lambda$  are listed in the titles.

the calculation of  $B(\gamma, \mu = 0, n)$  in figure 6, for a wide range of  $\gamma$  and for spherical ( $n = 3$ ) and cylindrical symmetries ( $n = 2$ ). Except for a few cases, the agreement is better than  $10^{-5}$ , and mostly to all digits given Ref [3]. In figure 7 we present the value  $\frac{\gamma-1}{\gamma+1}B$  as a function of  $\gamma$  for various values of  $\mu$ . In table I we list the numerical values of  $B$  for  $\gamma = 1.4, \frac{5}{3}$  for several values of  $\mu$ . Finally, In figure 8 the self similar profiles  $V(x), C(x), R(x)$  are shown for several examples.

#### IV. COMPARISON WITH HYDRODYNAMIC SIMULATIONS

In this section we compare the semi-analytical diverging shock solutions to numerical hydrodynamic simulations. As in Ref. [25], we employ a standard staggered-mesh artificial-viscosity one-dimensional Lagrangian code (for details, see Appendix D. in Ref. [25]).

We define two types of setups: (i) an initialization of a diverging shock flow, which propagates outwards and (ii) an initialization of an incoming shock flow which first converges to the origin and reflects outwards as a diverging shock which propagates outward into the converging shock flow. The latter case tests the ability of the simulation to accurately describe both the focusing of the shock at the center and the generation of the reflected shock, which then propagates into the incoming shock profile. The former case is more simple, as it does not include the shock focusing and reflection, but is still non-trivial

as it describes the propagation of the outgoing shock.

As was done in the case for the converging shock [25], we employ a piston velocity boundary condition, where the velocity is obtained from the analytic solution for the (converging and diverging) Guderley problem [37], that is, if the location of the piston is  $r_p(t)$ , its velocity which is externally applied is given by:

$$u_p(t) = u_{\text{analytic}}(r_p(t), t),$$

where  $u_{\text{analytic}}$  is the analytic velocity profile (equation 12) and the position of the piston is calculated in the Lagrangian simulation as the position of the outermost cell vertex. All simulations are initialized on a spatially uniform radial grid.

The hydrodynamics profiles are compared using relative  $L_p$  norms which are defined as follows:

$$L_p(y, y^{\text{analytic}}, v) = \frac{\left( \sum_i v_i |y_i - y_i^{\text{analytic}}|^p \right)^{\frac{1}{p}}}{\left( \sum_i v_i |y_i|^p \right)^{\frac{1}{p}} + \left( \sum_i v_i |y_i^{\text{analytic}}|^p \right)^{\frac{1}{p}}}, \quad (41)$$

where  $v_i$  is the volume of cell  $i$ , and  $y_i, y_i^{\text{analytic}}$  represent, respectively, the numerical and (semi)analytical hydrodynamic profiles.

We define 3 test cases:

1.  $\gamma = 1.4, \mu = 0$  - this is the canonical Guderley problem with a uniform initial density profile.



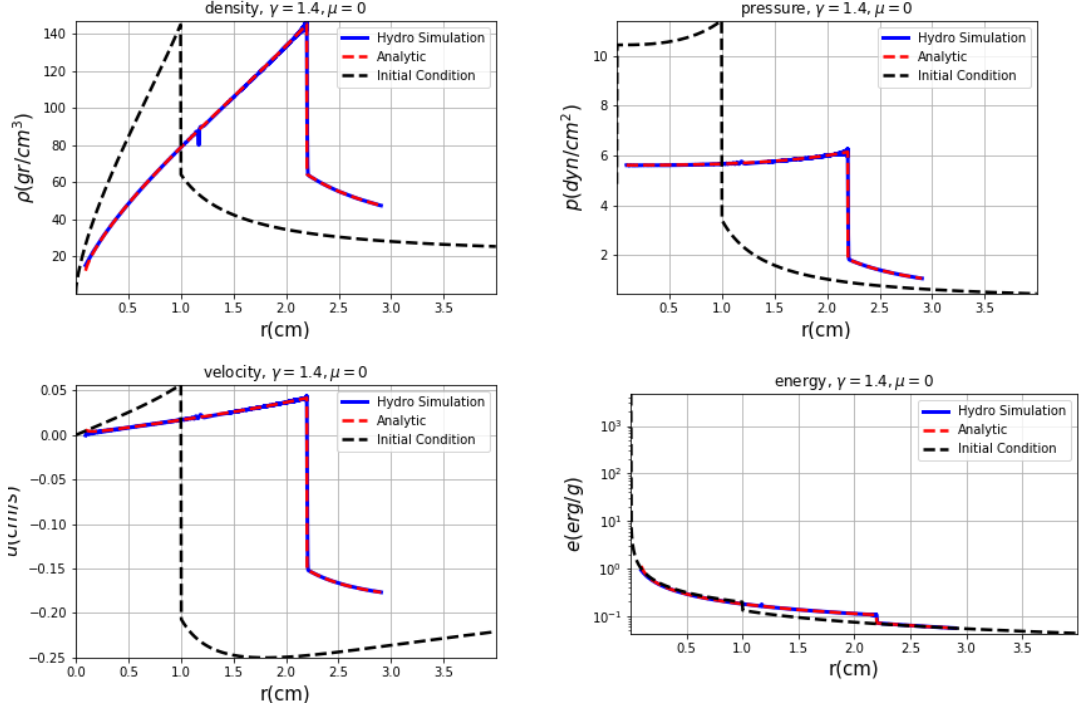


Figure 9. A comparison between the analytical solution (dashed red lines) and a numerical hydrodynamic simulation (blue lines) for  $\gamma = 1.4$ ,  $\mu = 0$ ,  $n = 3$  of the hydrodynamic profiles (as listed in the titles), for the initially diverging shock setup, in which the simulation is initialized with the analytic profiles shown in the dashed black lines at time  $t = B = 2.688$ , and evolves to time  $t = 2B$ . The simulation was carried out with 1000 computational cells.

2.  $\gamma = 2$ ,  $\mu = 0.5$  - a test case with a monotonically outward-increasing density profile. While the converging shock accelerates inward in such a profile, We expect the diverging shock to decelerate, as it advances into a denser material.
3.  $\gamma = 1.2$ ,  $\mu = -0.8$  - a test case with a monotonically decreasing density profile. In this case the opposite occurs: the converging shock decelerates on its way inwards, and the diverging shock accelerates, as it advances into an increasingly rarefied material.

Notably, a sharp discontinuity appears in the hydrodynamic profiles in all three cases (figures 9-11 and 15-17). As discussed in Ref. [25], these discontinuities exist over a single computational cell and were originated due to the presence of discontinuities in the initial hydrodynamic profiles [38]. As seen in the figures, they do not affect the overall stability and accuracy of the simulations. A detailed analysis of such initialization errors can be found in Ref. [4].

As in Ref. [25], we see that while there exists some variability in the accuracy of the simulations regarding the different physical quantities, we observe that a grid of 1000 computational cells will generally suffice to ensure an accuracy of a few percent or even less than one percent in all physical quantities at the end of the simulation. The spatial convergence rates (reduction of error

w.r.t. the analytical solution as a function of increase in grid size) is similar for all physical quantities in all simulations. These rates are all of order unity (as seen explicitly in figures 14 and 20), which is to be expected for an artificial viscosity numerical scheme, which is first order accurate in the presence of shocks.

#### A. Initialization as a Diverging Shock

As in the converging shock setup defined in Refs. [25, 34, 36], we initialize the simulation with density, velocity and pressure profiles given by the analytical diverging solution at time  $t = B$ , where the diverging shock is at  $r = 1$ . We let the flow evolve until the time  $t = 2B$ .

For each case we present the following plots: hydrodynamic profiles at the final time  $t = 2B$  (figures 9-11), the shock position (figure 12), the applied piston boundary condition (figure 13), the convergence of  $L_1$  norms for  $\rho, p, u, e$  (figure 14), and the convergence of  $\lambda, B$  which are calculated from the simulation using a fit of the shock position to the form  $(\frac{t}{B})^{\frac{1}{\lambda}}$ .

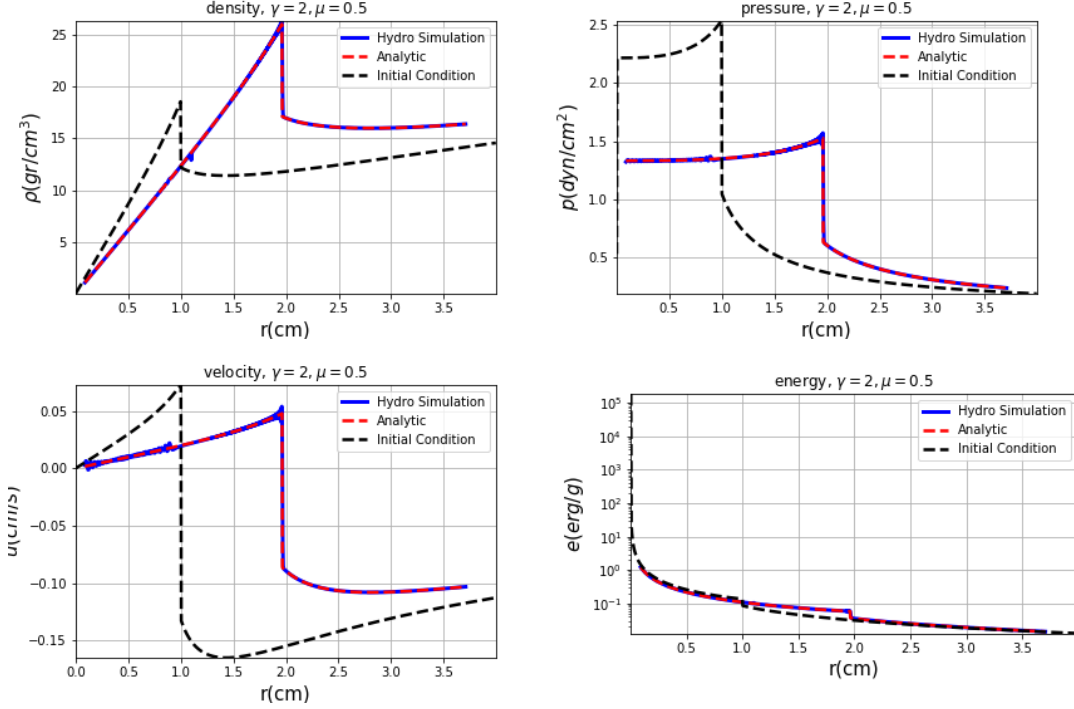


Figure 10. Same as figure 9, for the case  $\gamma = 2, \mu = 0.5$ , for which the initial time is  $t = B = 1.324$ .

### B. Initialization as a Converging Shock

In this setup, we initialize the simulation with density, velocity and pressure profiles given by the analytical converging solution at time  $t = -1$ , where the converging shock is at  $r = 1$ . We let the flow evolve as the shock reaches the center at time  $t = 0$  and reflects outwards, until it reaches the position  $r = 1$  at time  $t = B$ . For each case we present the following plots: density and pressure profiles at the final time  $t = B$  (figures 15-17), the converging and diverging shock position as function of time (figure 18), the applied piston boundary condition (figure 19), the convergence of  $L_1$  norms for  $\rho, p, u, e$  (figure 20), and the convergence of the diverging shock parameters  $\lambda_{\text{out}}, B$  which are calculated from the simulation using a fit of the diverging shock position to the form  $(\frac{t}{B})^{\frac{1}{\lambda}}$  for  $t > 0$ , and the converging shock exponent  $\lambda_{\text{in}}$ , which is calculated from the simulation using a fit of the converging shock position to the form  $(-t)^{\frac{1}{\lambda}}$  for  $t < 0$ .

## V. SUMMARY

In this work we studied in detail the complete Guderley problem of a converging and then diverging shock in an ideal gas medium with an initial power-law density profile,  $\rho(r) \sim r^\mu$ . We extend our previous work in Ref.

[25], which was dedicated to a detailed study of the converging shock. We presented the theoretical framework required to construct exact self-similar solutions for the converging and diverging flows. A generalized algorithm for a numerical calculation of the semi-analytical similarity solutions was developed. The diverging shock solution was studied in a wide range of parameters, namely the adiabatic constant  $\gamma$ , the initial density exponent  $\mu$  and for spherical and cylindrical symmetries. The results are in excellent agreement with previous published work, which, to the best of our knowledge, are only given for the case of an initially constant density profile ( $\mu = 0$ ).

The semi-analytic solutions were used to define non-trivial compressible flow problems which could serve for code verification. The solutions were compared to hydrodynamic simulations employing a one dimensional Lagrangian hydrodynamic code, by applying appropriate initial and boundary conditions. A very good agreement was reached between numerical hydrodynamic simulations and the semi-analytical solutions. This success highlights the use of the solutions for the purpose of verification and validation of numerical hydrodynamics simulation codes.

### Availability of data

The data that support the findings of this study are available from the corresponding author upon reasonable request.

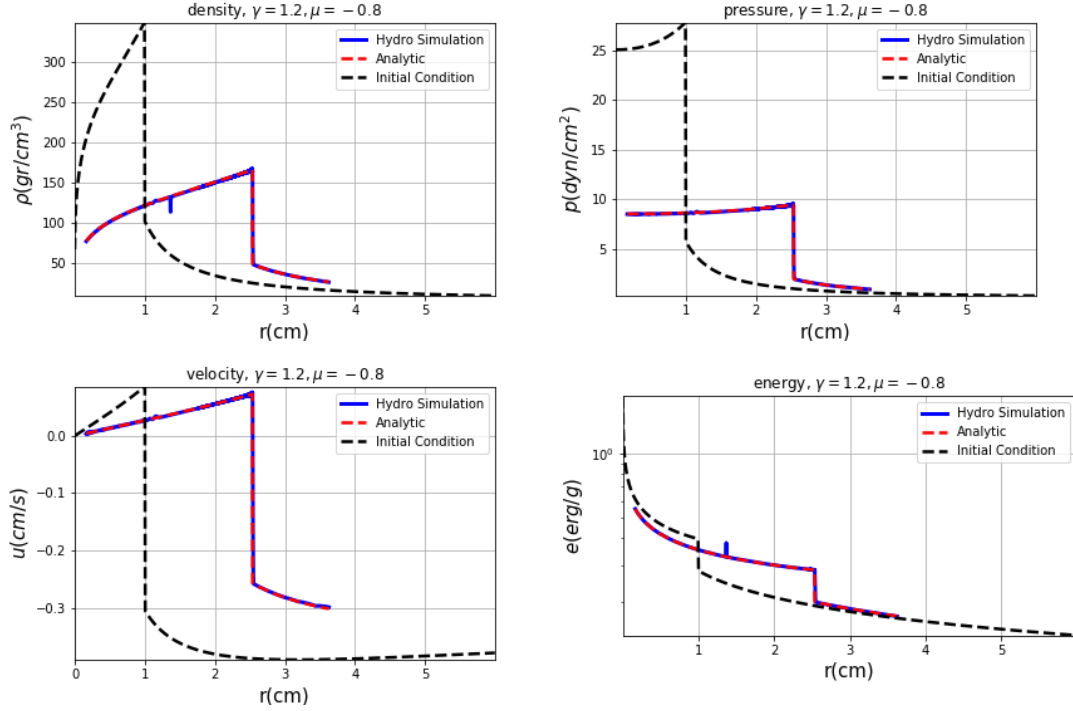


Figure 11. Same as figure 9, for the case  $\gamma = 1.2, \mu = -0.8$ , for which the initial time is  $t = B = 3.418$ .

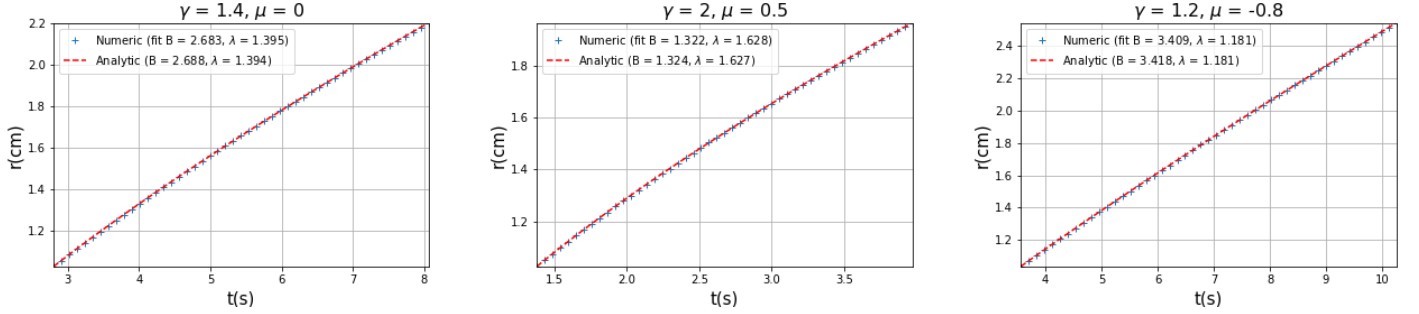


Figure 12. A comparison for the shock position as a function of time, between the analytical solution (red dashed line) and hydrodynamic simulations (crosses), for the simulations presented in figures 9-11 (as listed in the titles). We list in the legends the analytic and simulated results for the values of  $B, \lambda$ , which are obtained from the simulation by fitting to shock position to  $(t/B)^{\frac{1}{\lambda}}$ .

- 
- [1] KG Guderley. Starke kugelige und zylindrische verdichtungsstosse in der nahe des kugelmittelpunktes bnw. der zylinderachse. *Luftfahrtforschung*, 19:302, 1942.
  - [2] RB Lazarus and RD Richtmyer. Similarity solutions for converging shocks. Technical report, Los Alamos National Lab.(LANL), Los Alamos, NM (United States), 1977.
  - [3] Roger B Lazarus. Self-similar solutions for converging shocks and collapsing cavities. *SIAM Journal on Numerical Analysis*, 18(2):316–371, 1981.
  - [4] Scott D Ramsey, James R Kamm, and John H Bolstad. The Guderley problem revisited. *International Journal of Computational Fluid Dynamics*, 26(2):79–99, 2012.
  - [5] Akira Sakurai. On the problem of a shock wave arriving at the edge of a gas. *Communs. Pure and Appl. Math.*, 13, 1960.
  - [6] VD Sharma and Ch Radha. Similarity solutions for converging shocks in a relaxing gas. *International journal of engineering science*, 33(4):535–553, 1995.
  - [7] Nathalie Toqué. Self-similar implosion of a continuous stratified medium. *Shock Waves*, 11(3):157–165, 2001.
  - [8] JJ Ruby, JR Rygg, JA Gaffney, B Bachmann, and GW Collins. A boundary condition for Guderley’s converging shock problem. *Physics of Fluids*, 31(12):126104,

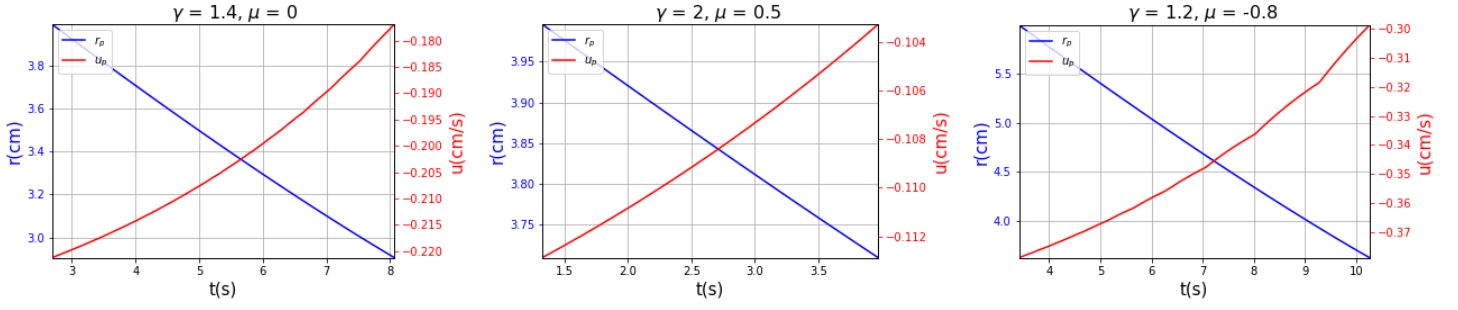


Figure 13. The piston boundary position (blue line, left axis) and applied velocity (red line, right axis) as a function of time, for the simulations presented in figures 9-11 (as listed in the titles).

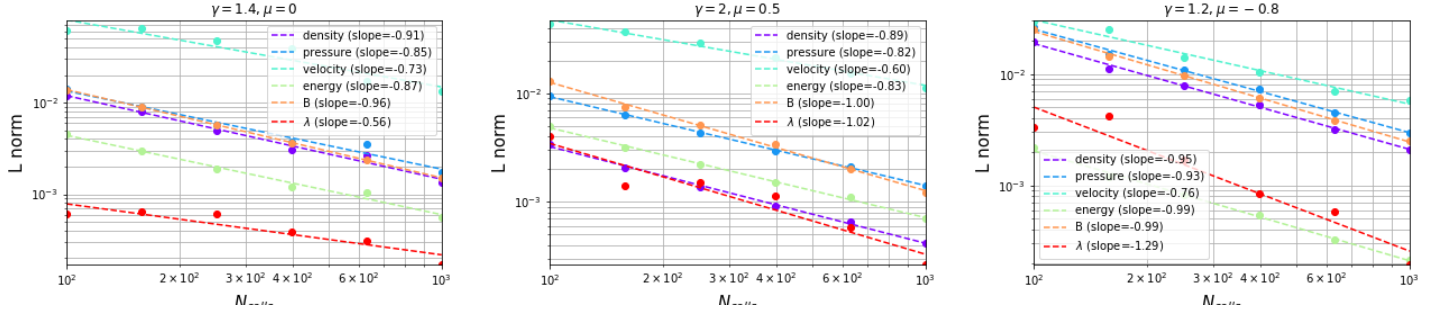


Figure 14. Numerical convergence of various quantities as a function of the number of cells for the cases presented in figures 9-11 (as listed in the titles). Shown are the relative  $L_1$  norms (see equation 41) for the density (purple), pressure (blue), velocity (cyan) and energy (green) profiles, as well as the relative errors for the fitted parameters  $B$  (orange) and  $\lambda$  (red). The points represent actual data and the dashed lines represent a log-log linear fit, whose resulting slope is listed in the legends. This slope represents the order of spatial convergence.

- 2019.
- [9] Anxo Biasi. Self-similar solutions to the compressible euler equations and their instabilities. *Communications in Nonlinear Science and Numerical Simulation*, 103:106014, 2021.
  - [10] Scott D Ramsey, Emma M Schmidt, Zachary M Boyd, Jennifer F Lilieholm, and Roy S Baty. Converging shock flows for a Mie-Grüneisen equation of state. *Physics of Fluids*, 30(4):046101, 2018.
  - [11] Mayank Singh, Astha Chauhan, Kajal Sharma, and Rajan Arora. Kinematics of one-dimensional spherical shock waves in interstellar van der Waals gas clouds. *Physics of Fluids*, 32(10):107109, 2020.
  - [12] Ankita Sharma and Rajan Arora. Similarity solutions for imploding strong shock waves in a van der Waals gas. *Partial Differential Equations and Applications*, 3(6):72, 2022.
  - [13] Andrés Calvo-Rivera, C Huete, and Alexander L Velikovich. The stability of expanding reactive shocks in a van der Waals fluid. *Physics of Fluids*, 34(4):046106, 2022.
  - [14] Deepika Singh, Antim Chauhan, and Rajan Arora. Convergence of strong shock waves in an ideal gas with dust particles. *Physics of Fluids*, 34(2):026106, 2022.
  - [15] Sergey G Chefranov, Yakov E Krasik, and Alexander Rososhek. Limitation in velocity of converging shock wave. *Physics of Fluids*, 34(1):016101, 2022.
  - [16] Antim Chauhan, Rajan Arora, and Amit Tomar. Piston driven converging shock waves in nonideal magnetogasdynamics of variable density. *Physics of Fluids*, 33(11):116110, 2021.
  - [17] Shalini Yadav, Deepika Singh, and Rajan Arora. Propagation of cylindrical shock waves in rotational axisymmetric dusty gas with magnetic field: Isothermal flow. *Physics of Fluids*, 33(12):127106, 2021.
  - [18] Gorakh Nath. Propagation of ionizing shock wave in a dusty gas medium under the influence of gravitational and azimuthal magnetic fields. *Physics of Fluids*, 34(8):083307, 2022.
  - [19] Helge Kristian Jenssen and Charis Tsikkou. Radially symmetric non-isentropic euler flows: continuous blowup with positive pressure. *Physics of Fluids*, 35(1):016117, 2023.
  - [20] Elaine S. Oran and Vadim N. Gamezo. Origins of the deflagration-to-detonation transition in gas-phase combustion. *Combustion and Flame*, 148(1-2):4, 2007.
  - [21] A Vallet, X Ribeyre, and V Tikhonchuk. Finite mach number spherical shock wave, application to shock ignition. *Physics of Plasmas*, 20(8):082702, 2013.
  - [22] H Abu-Shawareb, R Acree, P Adams, J Adams, B Addis, R Aden, P Adrian, BB Afeyan, M Aggleton, L Aghaian, et al. Lawson criterion for ignition exceeded in an inertial fusion experiment. *Physical Review Letters*, 129(7):075001, 2022.

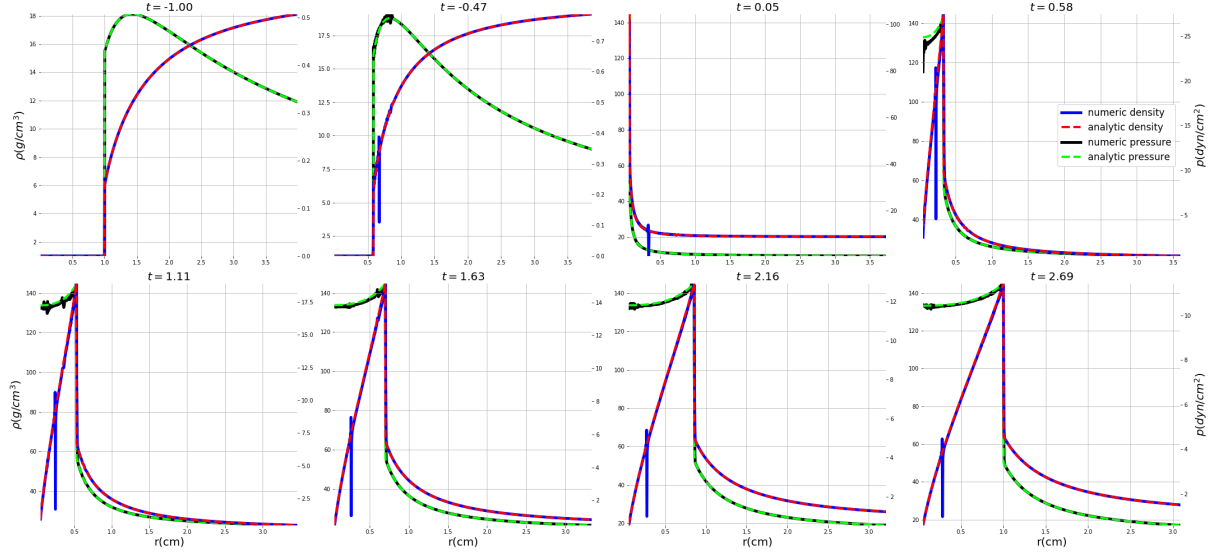


Figure 15. A comparison between the analytical solution and a numerical hydrodynamic simulation (with 1000 cells) for the density (left  $y$  axis, analytic - dashed red line, simulation - solid blue line) and pressure (right  $y$  axis, analytic - dashed green line, simulation - solid black line) profiles for the converging shock setup and for  $\gamma = 1.4$ ,  $\mu = 0$ . The simulation is initialized with the analytic converging shock profiles at time  $t = -1$  where the converging shock front is at  $r = 1$ . We let the flow evolve as the shock reaches the center at time  $t = 0$  and reflects outwards, until it reaches the position  $r = 1$  at the final time  $t = B = 2.684$  (see also figure 18). The simulation was carried with 1000 computational cells.

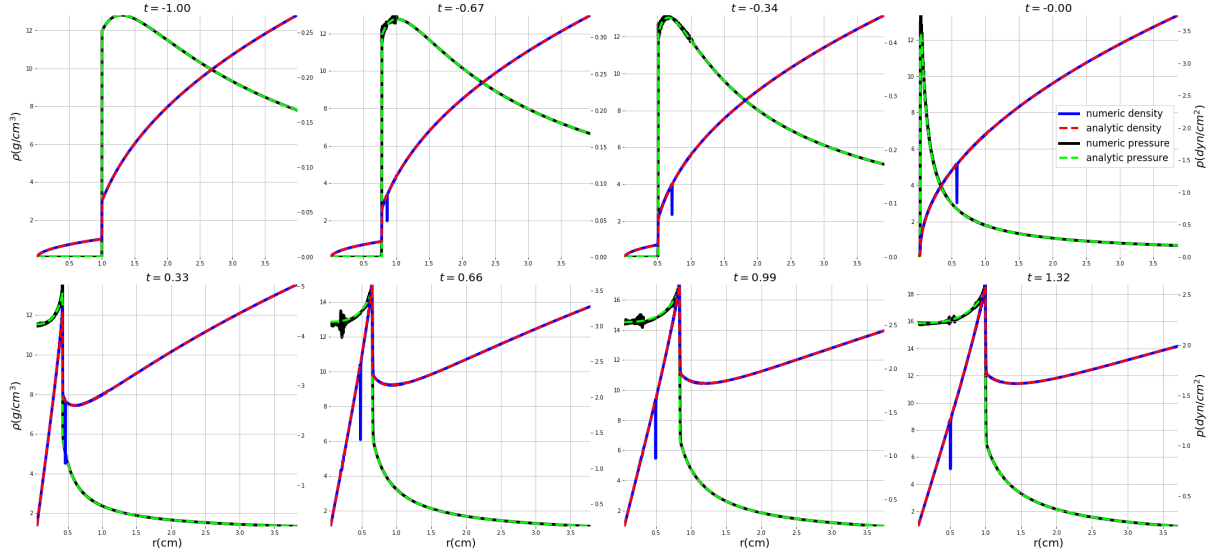


Figure 16. Same as figure 15, for the case  $\gamma = 2$ ,  $\mu = 0.5$ , for which the final time is  $t = B = 1.324$ .

- [23] Doron Kushnir, Eli Livne, and Eli Waxman. Imploding ignition waves. i. one-dimensional analysis. *The Astrophysical Journal*, 752(2):89, 2012.
- [24] Ken J. Shen and Lars Bildsten. The ignition of carbon detonations via converging shocks in white dwarfs. *The Astrophysical Journal*, 785(2):61, 2014.
- [25] Itamar Giron, Shmuel Balberg, and Menahem Krief. Solutions of the imploding shock problem in a medium with varying density. *Physics of Fluids*, 33(6):066105, 2021.
- [26] F.L Chernous'ko. A converging shock-wave in a gas of variable density. *Journal of Applied Mathematics and Mechanics*, 24(5):1334–1348, 1960.

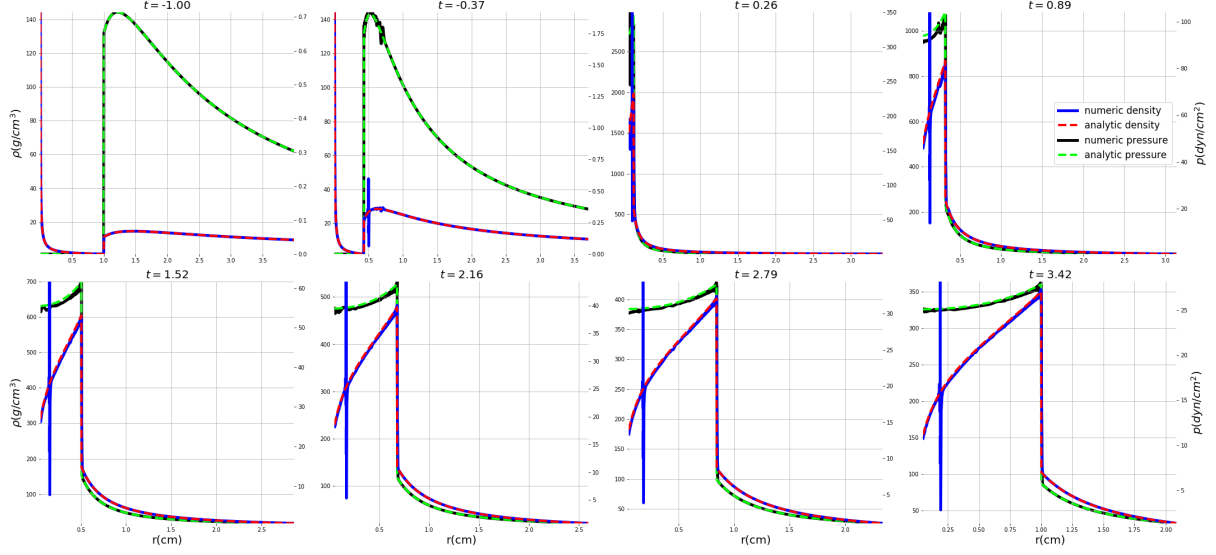


Figure 17. Same as figure 9, for the case  $\gamma = 1.2, \mu = -0.8$ , for which the final time is  $t = B = 3.418$ .

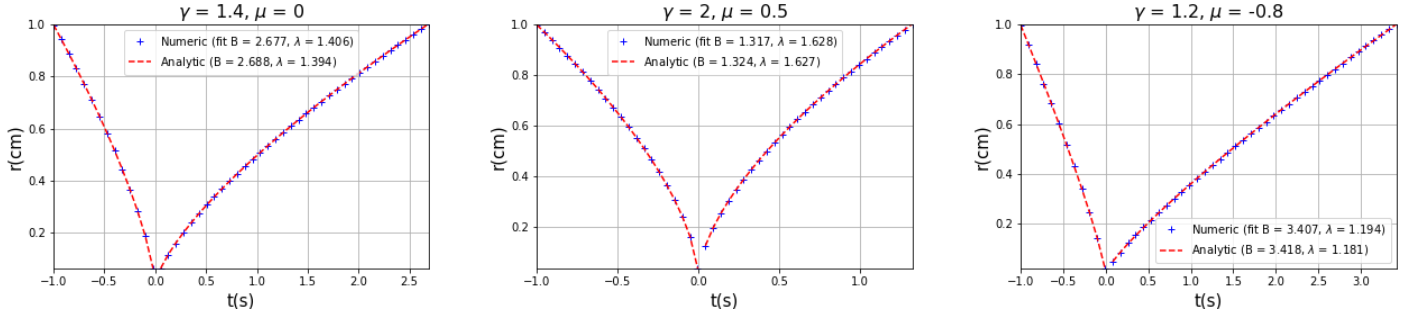


Figure 18. A comparison for the shock position as a function of time, between the analytical solution (red dashed line) and hydrodynamic simulations (crosses), for the simulations presented in figures 15-17 (as listed in the titles). We list in the legends the analytic and simulated results for the values of  $B, \lambda$ , which are obtained from the simulation by fitting to diverging shock position ( $t > 0$ ) to  $(t/B)^{\frac{1}{\lambda}}$ .

- [27] Elisha Modelevsky and Re'em Sari. Revisiting the strong shock problem: Converging and diverging shocks in different geometries. *Physics of Fluids*, 33(5):056105, 2021.
- [28] Ya B Zel'Dovich and Yu P Raizer. *Physics of shock waves and high-temperature hydrodynamic phenomena*. Courier Corporation, 2002.
- [29] James R Kamm. Evaluation of the Sedov-von Neumann-Taylor blast wave solution. *Astrophys. J. Suppl.(submitted)*, page 46, 2000.
- [30] Menahem Krief. Analytic solutions of the nonlinear radiation diffusion equation with an instantaneous point source in non-homogeneous media. *Physics of Fluids*, 33(5):057105, 2021.
- [31] Menahem Krief. Piston driven shock waves in non-homogeneous planar media. *Physics of Fluids*, 35(4), 2023.
- [32] RF Chisnell. An analytic description of converging shock waves. *Journal of Fluid Mechanics*, 354:357–375, 1998.
- [33] JP Vishwakarma and Subhash Vishwakarma. An analytic description of converging shock waves in a gas with variable density. *Physica Scripta*, 72(2-3):218, 2005.
- [34] Scott D Ramsey and Mikhail J Shashkov. Simulation and analysis of converging shock wave test problems. Technical report, Los Alamos National Lab.(LANL), Los Alamos, NM (United States), 2012.
- [35] Scott D Ramsey and Mikhail J Shashkov. Surrogate Guderley test problem definition. Technical report, Los Alamos National Lab.(LANL), Los Alamos, NM (United States), 2012.
- [36] Scott D Ramsey and Jennifer F Lilieholm. Verification assessment of piston boundary conditions for Lagrangian simulation of the Guderley problem. *Journal of Verification, Validation and Uncertainty Quantification*, 2(3), 2017.
- [37] Scott D Ramsey and Roy S Baty. Piston driven converging shock waves in a stiffened gas. *Physics of Fluids*, 31(8):086106, 2019.



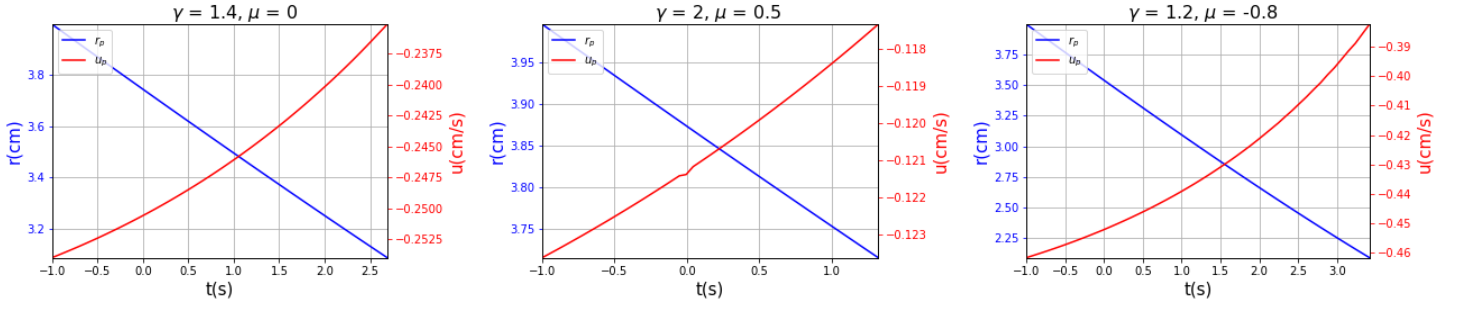


Figure 19. The piston boundary position (blue line, left axis) and applied velocity (red line, right axis) as a function of time, for the simulations presented in figures 15-17 (as listed in the titles).

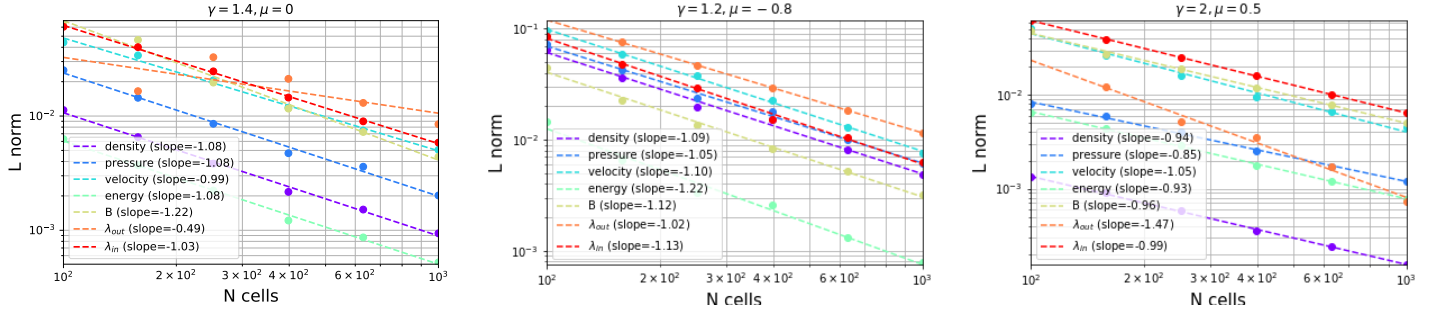


Figure 20. Numerical convergence of various quantities as obtained from the simulation to the analytical solution, a function of the number of cells for the cases presented in figures 15-17 (as listed in the titles). Shown are the relative  $L_1$  norms (see equation 41) for the density (purple), pressure (blue), velocity (cyan) and energy (green) profiles, as well as the relative errors for the fitted diverging shock position parameters  $B$  (yellow) and  $\lambda_{out}$  (orange) and the converging shock parameter  $\lambda_{in}$  (red), according to equation 21. The points represent actual data and the dashed lines represent a log-log linear fit, whose resulting slope is listed in the legends. This slope represents the order of spatial convergence.

[38] Randall J LeVeque et al. *Finite volume methods for hyperbolic problems*, volume 31. Cambridge university press, 2002.

## Appendix A: Rankine-Hugoniot Jump Relations

In this appendix we use the similarity representation 12-14, in order to write the dimensional Rankine-Hugoniot jump relations 7-9 for the diverging shock, in terms of the similarity profiles. We note that the location of the diverging shock varies according to the power law  $r_s(t) = (\frac{t}{B})^{\frac{1}{\lambda}}$ . Hence the shock velocity in the jump relations 7-9 is  $D = \frac{dr_s}{dt} = \frac{r_s}{\lambda t}$ .

The mass equation 7 reads:

$$\frac{\rho_0 r_s^{1+\mu}}{\lambda t} (R_2 - R_1) = \frac{\rho_0 r_s^{1+\mu}}{\lambda t} R_1 V_1 - \frac{\rho_0 r_s^{1+\mu}}{\lambda t} R_2 V_2,$$

where, as expected, all dimensional quantities drop, and we obtain the first dimensionless jump condition:

$$R_2 (1 + V_2) = R_1 (1 + V_1). \quad (A1)$$

Dividing the momentum equation 8 by the continuity equation 7 and writing the pressure in terms of the speed of sound, we get after some straightforward algebra:

$$u_1 - u_2 = \frac{1}{\gamma} \left( \frac{c_2^2}{u_2 - D} - \frac{c_1^2}{u_1 - D} \right).$$

Next, expressing this equation in terms of the specific enthalpy  $h = e + \frac{p}{\rho} + \frac{1}{2} (u - D)^2$ , which is constant across the shock, we obtain:

$$\frac{1}{(u_1 - D)(u_2 - D)} = \frac{\gamma + 1}{2(\gamma - 1)h}. \quad (A2)$$

This last relation is then used for  $u_2 - D$ :

$$u_2 - D = \frac{\gamma - 1}{\gamma + 1} (u_1 - D) + \frac{2c_1^2}{(\gamma + 1)(u_1 - D)}.$$

Finally, we substitute the shock velocity and use the similarity representation 12-13:

$$-\frac{r_s}{\lambda t} V_2 - \frac{r_s}{\lambda t} = \frac{\gamma - 1}{\gamma + 1} \left( -\frac{r_s}{\lambda t} V_1 - \frac{r_s}{\lambda t} \right) + \frac{2 \left( -\frac{r_s}{\lambda t} C_1 \right)^2}{(\gamma + 1) \left( -\frac{r_s}{\lambda t} V_1 - \frac{r_s}{\lambda t} \right)}$$

As expected, all dimensional quantities drop and we obtain the second dimensionless jump condition:

$$1 + V_2 = \frac{\gamma - 1}{\gamma + 1} (1 + V_1) + \frac{2C_1^2}{(\gamma + 1)(1 + V_1)}. \quad (\text{A3})$$

In order to obtain the third dimensionless jump condition, we write:

$$\frac{p}{\rho} = \frac{c^2}{\gamma} = \frac{r^2 C^2}{\gamma \lambda^2 t^2}, \quad (\text{A4})$$

and derive for the specific energy

$$e = \frac{p}{(\gamma - 1)\rho} = \frac{r^2 C^2}{\gamma(\gamma - 1)\lambda^2 t^2}. \quad (\text{A5})$$

Substituting this result in the energy jump condition (equation 9) leads to:

$$\begin{aligned} & \frac{r_s^2 C_1^2}{\gamma(\gamma - 1)\lambda^2 t^2} + \frac{r_s^2 C_1^2}{\gamma \lambda^2 t^2} + \frac{1}{2} \left( -\frac{r_s}{\lambda t} V_1 - \frac{r_s}{\lambda t} \right)^2 \\ &= \frac{r_s^2 C_2^2}{\gamma(\gamma - 1)\lambda^2 t^2} + \frac{r_s^2 C_2^2}{\gamma \lambda^2 t^2} + \frac{1}{2} \left( -\frac{r_s}{\lambda t} V_2 - \frac{r_s}{\lambda t} \right)^2 \end{aligned}$$

and as before, all dimensional quantities drop and we obtain the third dimensionless jump condition:

$$C_2^2 = C_1^2 + \frac{\gamma - 1}{2} \left( (1 + V_2)^2 - (1 + V_1)^2 \right). \quad (\text{A6})$$